Check for updates

Structural insights into the mechanism of pancreatic K$_{ATP}$ channel regulation by nucleotides

Mengmeng Wang [1,2,3,4], Jing-Xiang Wu[1,4], Dian Ding[1,2,3,4] & Lei Chen [1,2,3,4]✉

ATP-sensitive potassium channels (K$_{ATP}$) are metabolic sensors that convert the intracellular ATP/ADP ratio to the excitability of cells. They are involved in many physiological processes and implicated in several human diseases. Here we present the cryo-EM structures of the pancreatic K$_{ATP}$ channel in both the closed state and the pre-open state, resolved in the same sample. We observe the binding of nucleotides at the inhibitory sites of the Kir6.2 channel in the closed but not in the pre-open state. Structural comparisons reveal the mechanism for ATP inhibition and Mg-ADP activation, two fundamental properties of K$_{ATP}$ channels. Moreover, the structures also uncover the activation mechanism of diazoxide-type K$_{ATP}$ openers.

[1] State Key Laboratory of Membrane Biology, College of Future Technology, Institute of Molecular Medicine, Peking University, Beijing Key Laboratory of Cardiometabolic Molecular Medicine, 100871 Beijing, China. [2] Peking-Tsinghua Center for Life Sciences, Peking University, 100871 Beijing, China. [3] Academy for Advanced Interdisciplinary Studies, Peking University, 100871 Beijing, China. [4] National Biomedical Imaging Center, Peking University, 100871 Beijing, China. ✉email: chenlei2016@pku.edu.cn

The activity of K_{ATP} channels is inhibited by cytosolic ATP and activated by Mg-ADP[1]. The opening of K_{ATP} channels leads to the hyperpolarization of the cell, while the inhibition of K_{ATP} results in depolarization[2]. Therefore, K_{ATP} channels translate the cellular metabolic status into the excitability of the plasma membrane to control the electrical activity of the cell[1]. Because of its unique properties, K_{ATP} channels play essential roles in many key physiological processes, such as hormone secretion[2], cardiac preconditioning[3], and vasodilation[4]. The genetic mutations of genes encoding K_{ATP} channels lead to a spectrum of diseases, ranging from metabolic syndrome to cardiovascular diseases and CNS disorders, including neonatal diabetes or even the Developmental delay, Epilepsy, and Neonatal Diabetes" (DEND) syndrome[5], hyperinsulinaemic hypoglycemia of infancy[5], dilated cardiomyopathy[6], familial atrial fibrillation[7], Cantú syndrome[8,9] and intellectual disability myopathy syndrome[10]. K_{ATP} channels are also important drug targets. K_{ATP} inhibitors promote insulin release to treat diabetes. These drugs include glibenclamide (GBM) and repaglinide (RPG), the so-called insulin secretagogues[11]. K_{ATP} activators (K_{ATP} openers) are used to pharmacologically activate K_{ATP} channels in clinic[12]. Diazoxide is an oral K_{ATP} opener and has been used in the treatment of hypoglycemia and hypertension for nearly half a century[12].

Functional K_{ATP} channels are hetero-octamers composed of four Kir6 and four SUR subunits[13]. Kir6 are inward rectifier potassium channels that require $PI(4,5)P_2$ for maximum activity[14–18]. It harbors the nucleotide-binding pocket which can bind the inhibitory ATP, and also ADP to a lesser extent[14,19]. SUR subunits are ABC transporter-like proteins that undergo Mg-nucleotide-dependent conformational changes[20]. The SUR subunits bind to activating Mg-ADP and drugs, including insulin secretagogues and K_{ATP} openers[11,21]. Recent advances in cryo-EM structure determination of K_{ATP} channels in the presence of different ligand combinations by three groups have provided instrumental information about how K_{ATP} channels are assembled from individual subunits, how inhibitory ATP binds the channel, and how chemically distinct insulin secretagogues bind at SUR subunits[22–28]. Moreover, the conformational changes of the SUR1 subunit upon Mg-nucleotide binding have been visualized[22,26,29]. Despite the progress, the fundamental questions about how K_{ATP} channels work, including the mechanism of ATP inhibition and Mg-ADP activation, remain elusive. In this work, we obtain the structures of the K_{ATP} channel in both the closed state and the pre-open state, revealing the mechanism of K_{ATP} channel regulation by nucleotides.

Results

Structure determination. $PI(4,5)P_2$ is a signaling lipid important for K_{ATP} channel activity[14–18]. However, previous attempts of supplementing soluble $PI(4,5)P_2$ analog $PI(4,5)P_2diC_8$ into K_{ATP} cryo-EM sample failed to stabilize the channel in the open state, and no $PI(4,5)P_2diC_8$ density was observed[22,26]. In contrast, there are several structures of other Kir family members with $PI(4,5)P_2diC_8$ bound available, including Kir2.2[30] or Kir3.2[31]. Therefore, we hypothesized the affinity of $PI(4,5)P_2diC_8$ for Kir6.2 might be lower than those of Kir2.2 or Kir3.2. In agreement with it, sequence alignments showed several positively charged residues at the $PI(4,5)P_2$ binding pocket of Kir2.2 or Kir3.2 are replaced by non-charged polar residues in Kir6 channels (Supplementary Fig. 1a). Particularly, the positively charged Lys residues were replaced by Asn at 41 and by His at 175 (Supplementary Fig. 1a). To enhance the binding affinity of $PI(4,5)P_2diC_8$ toward Kir6.2, we made mutations N41K and H175K on Kir6.2. Neomycin is a polyvalent cation that can bind and dissociate $PI(4,5)P_2$ from

Kir6.2[32] and high neomycin sensitivity is correlated with low $PI(4,5)P_2$ affinity[32]. Therefore, we exploited the neomycin sensitivity assay to evaluate the $PI(4,5)P_2$ affinity of Kir6.2 mutants. We found that the H175K mutation significantly reduced the neomycin sensitivity, indicating an enhanced $PI(4,5)P_2$ affinity (Fig. 1a and Supplementary Fig. 1b). Further analysis showed that H175K mutant can be inhibited by ATP and activated by Mg-ADP and NN414 (Fig. 1b), which is a high-affinity diazoxide-type K_{ATP} opener (Supplementary Fig. 1c)[33].

Based on these observations, we made H175K mutation on the SUR1-Kir6.2 fusion constructs, in which the C terminus of SUR1 is covalently linked to the N terminus of Kir6.2 by a long linker to ensure the correct 4:4 stoichiometry between Kir6.2 and SUR1[26], yielding the $H175K_{cryo-EM}$ construct. The $H175K_{cryo-EM}$ construct can be inhibited by ATP and activated by Mg-ADP and NN414 (Supplementary Fig. 1d). These results suggest that $H175K_{cryo-EM}$ recapitulates the basic electrophysiological properties of the wild-type K_{ATP} channel and could be used for structural studies. We purified $H175K_{cryo-EM}$ protein in detergent and supplemented Mg-ADP, $PI(4,5)P_2diC_8$, and NN414 into the protein for cryo-EM sample preparation (Supplementary Fig. 1e, f).

Single particle cryo-EM analysis showed the $H175K_{cryo-EM}$ protein shows the "propeller" shape (Fig. 1c–e, and Supplementary Figs. 2, 3), similar to our previous wild-type K_{ATP} protein in a similar condition[26]. The consensus refinement revealed that the peripheral ABC transporter modules of the SUR1 subunit (TMD1-NBD1-TMD2-NBD2) show motions relative to the central K_{ATP} channel core, consisting of Kir6.2 and SUR1-TMD0 domains. We further exploited symmetry expansion, signal subtraction, and local refinement to improve the resolution of the ABC transporter module to 3.1 Å[26] (Supplementary Fig. 2). The focused 3D classification revealed that the K_{ATP} channel core has obvious conformational heterogeneity at the bundle crossings of the Kir6.2 channel, showing a close to open transition at the gate. Subsequent refinement resolved two 3D classes: one class has a closed and the other has a widened inner helix gate. The resolution of them reached 3.16 Å and 2.87 Å for the Kir6.2 channel after focused refinement, respectively (Supplementary Fig. 2). The maps obtained from local refinement were aligned to consensus maps and combined to yield two composite maps for model building and interpretation (Supplementary Figs. 2, 3, and Supplementary Table 1).

Conformational changes of Kir6.2 TMD during channel opening. The structure of Kir6.2 in the closed state of $H175K_{cryo-EM}$ is similar to our previous ATP + RPG state structure (PDB ID: 6JB1)[27], with a root-mean-square deviation (RMSD) of 0.7198 Å (Fig. 2 and Supplementary Fig. 4). Residues on the M2 helix tightly seal the pore at the bundle crossing (Fig. 2a, b). The side chains of L164 and F168 form the gate, where the radius of the narrowest restriction is below 1 Å (Fig. 2a, b, e). In contrast, in the structure with widened gate, the inner part of the M2 helix moves outward (Fig. 2c, d). Particularly, the side chains of L164 and F168 move away from the center, resulting in the dilation of the pore (Fig. 2c, d, f, g). The radius of the ion permeation pathway at the bundle crossing of TMD now increases to 3 Å (Fig. 2e). However, the constriction at the cytosolic G-loop gate still shows a radius of 2.6 Å (Fig. 2e). Although the Kir6.2 channel in this structure is not fully open compared to the CNG channel (PDB ID: 6WEK)[34] and does not allow the passage of fully hydrated potassium ions with estimated radii of 3.3 Å[35], the channel is clearly in transition to the open state. Therefore, we tentatively assign the current structure with the widened gate as the "pre-open" state.

Associated with the expansion of the pore at the center, are concomitant movements of the inner part of the Interfacial
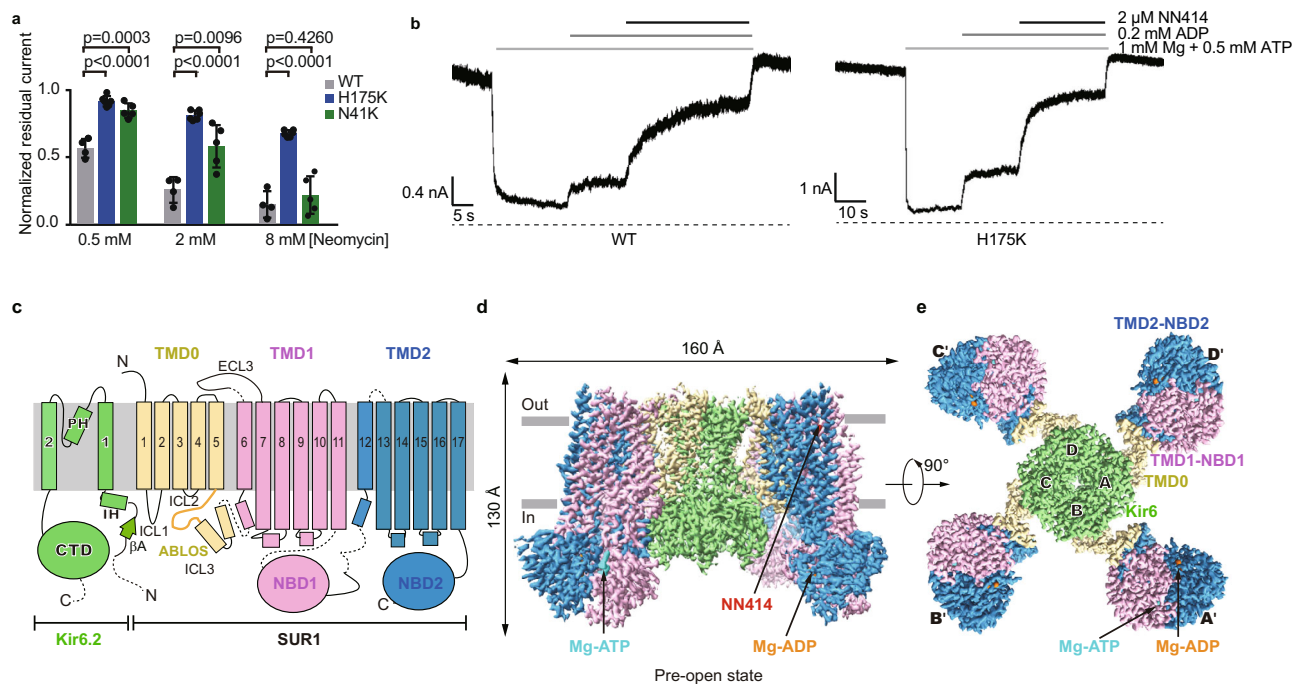
Fig. 1 Structure of the pancreatic K_{ATP} channel (H175K$_{cryo-EM}$) in the pre-open state. a Neomycin inhibition of the inside-out currents of the K_{ATP} channel. Wild type (WT), H175K, and N41K mutants of Kir6.2 were co-expressed with wild type SUR1 for recordings. Data are shown as mean ± SD. WT $n = 4$, H175K $n = 6$, N41K $n = 5$ independent patches, respectively. p values were calculated by unpaired two-tailed t-test and were indicated above. **b** Representative inside-out recordings of K_{ATP} channel formed by the wild-type Kir6.2 or the H175K mutant. **c** Topology of Kir6.2 and SUR1 subunits. PH, pore helix; ECL, extracellular loop; ICL, intracellular loop; IH, interfacial helix; CTD, cytoplasmic domain; TMD, transmembrane domain; NBD, nucleotide-binding domain. Transmembrane helices are shown as cylinders. The phospholipid bilayer is shown as thick gray lines. Kir6.2, SUR1 TMD0-ICL3 fragment, TMD1-NBD1, and TMD2-NBD2 are shown in green, yellow, violet, and blue, respectively. **d** Side view of the K_{ATP} complex in the pre-open state. Mg-ADP, Mg-ATP, and NN414 are shown in orange, cyan, and red, respectively. **e** Bottom view of the K_{ATP} channel in the pre-open state from the intracellular side. Source data are provided as a Source Data file.

Helix (IH) and M1 helices (Fig. 2f, g). In the closed state, the side chains of F60 on IH pack against T171 on M2 stabilize the closed pore (Fig. 2f, g). While in the pre-open state, the side chains of F60 swing away, which allows the expansion of M2 (Fig. 2f, g). In contrast to the obvious structural rearrangements of the inner portion of the pore, the structure of the outer region of the pore, especially at the selectivity filter, has little change (Fig. 2g).

In the structure of Kir3.2 in complex with PI(4,5)P$_2$diC$_8$[31], the PI(4,5)P$_2$diC$_8$ molecules bind at the subunit interface at the inner leaflet of the membrane. We found lipid-like densities in both closed state and pre-open state of H175K$_{cryo-EM}$ at similar positions (Supplementary Fig. 3), but the lack of head group feature hindered confident identification of their identities. Therefore, whether PI(4,5)P$_2$diC$_8$ molecules were bound in the H175K$_{cryo-EM}$ structures awaits further investigation.

Conformational changes of Kir6.2 CTD during channel opening. In the closed state, there are ADP densities inside each nucleotide-binding pocket of Kir6.2 CTD (Supplementary Fig. 3). The binding mode of the adenosine group of ADP is similar to that observed previously[25–27]. In contrast, there is no ADP density in the pre-open state, and we observed an obvious structural reorganization around the nucleotide-binding pocket of Kir6.2 (Fig. 3). The conformation of R50-R54 on the βA-IH loop has large changes (Fig. 3a, b, and Supplementary Movie 1). The side chains of Q52 flip from a solvent-exposed conformation to a buried conformation, while the side chains of E51 move in the opposite direction, occupying the nucleotide-binding pocket (Fig. 3b, Supplementary Fig. 4g–h, and Supplementary Movie 1).

During channel opening, there is a 6° anti-clockwise rotation of CTD viewing from the intracellular side, resulting in the clash between E51 and the nucleotide-binding pocket in the pre-open state (Fig. 3c and Supplementary Fig. 4i). Therefore, the structure of Kir6.2 in the pre-open state is not compatible with the binding of nucleotides anymore, in agreement with the fact that no ADP was observed in the nucleotide-binding pocket of the pre-open state.

Conformational changes of SUR1 TMD0 domain during channel opening. TMD0 domain of SUR1 has a five-helix-bundle structure[23,25]. The N terminal region and TM1 of SUR1 TMD0 interact with the M1 helix of Kir6.2. The extracellular side of TMD0 harbors the docking groove for ECL3 of SUR1 ABC transporter module (335–347)[27]. We observed the outward movements of the TMD0 domain in the inner leaflet and cytosolic region (ICL1, ICL2, and ICL3) during channel opening, while the structure of TMD0 in the outer leaflet largely stays the same (Fig. 4a). These observations suggest the outer half of TMD0 is a structural scaffold that is responsible for tethering Kir6.2 with the ABC transporter module, while the inner half of TMD0 has conformational plasticity for regulatory function. In detail, part of the ICL1 (51-60) of TMD0 is disordered in the closed state, but it is ordered in the pre-open state and forms main-chain hydrogen bonding with βA of Kir6.2 CTD (Fig. 4a, b). In the RPG + ATP bound state structure (PDB ID: 6JB1), K205 on the ATP-binding loop of SUR1 (ABLOS) motif of ICL3 from TMD0 interacts with β and γ phosphates of ATP[27]. But in both the closed state and the pre-open state structures of
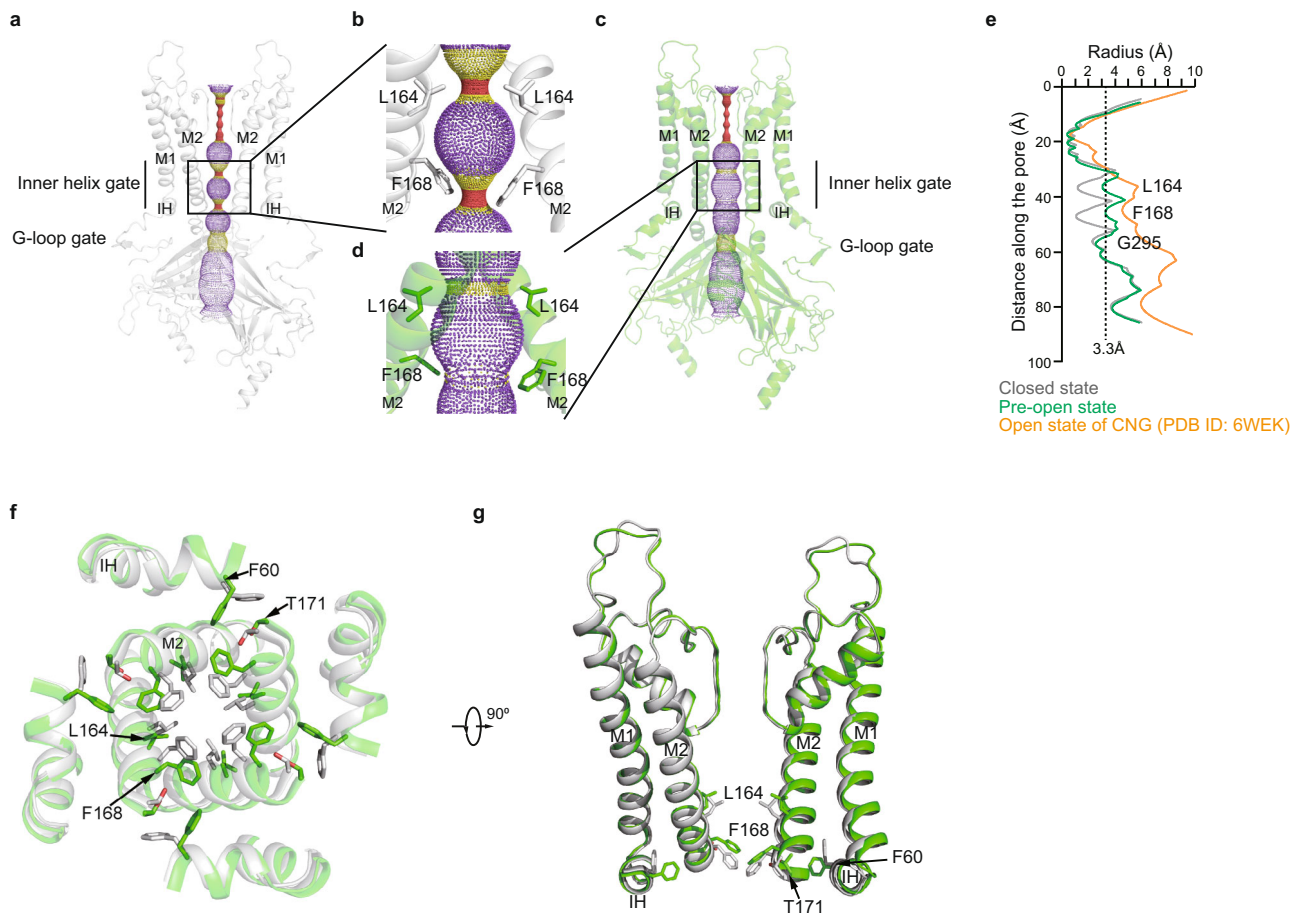
Fig. 2 The conformational changes of Kir6.2 TMD during K$_{ATP}$ channel opening. a Side view of Kir6.2 subunits of H175K$_{cryo-EM}$ in the closed state. The ion conduction pathway along the pore is shown as dots and colored as red, yellow, and purple according to the pore radii of <1.4, 1.4–3.3, and >3.3 Å. M1, M2, and IH are labeled. For clarity, the subunits in front and in the back were omitted. **b** Close-up view of M2 helices in (**a**) with gate residues shown as sticks (L164 and F168). **c** Side view of Kir6.2 subunits of H175K$_{cryo-EM}$ in the pre-open state. **d** Close-up view of M2 helices in (**c**). **e** Calculated pore profiles of the H175K$_{cryo-EM}$ closed state (gray), H175K$_{cryo-EM}$ pre-open state (green), and the open state of CNG channel (PDB ID: 6WEK) (orange). The size of a fully hydrated potassium ion (3.3 Å) is shown as dashes. **f** Structural comparison of the transmembrane domain between the closed state (gray) and the pre-open state (green). **g** A 90° rotated view of (**d**).
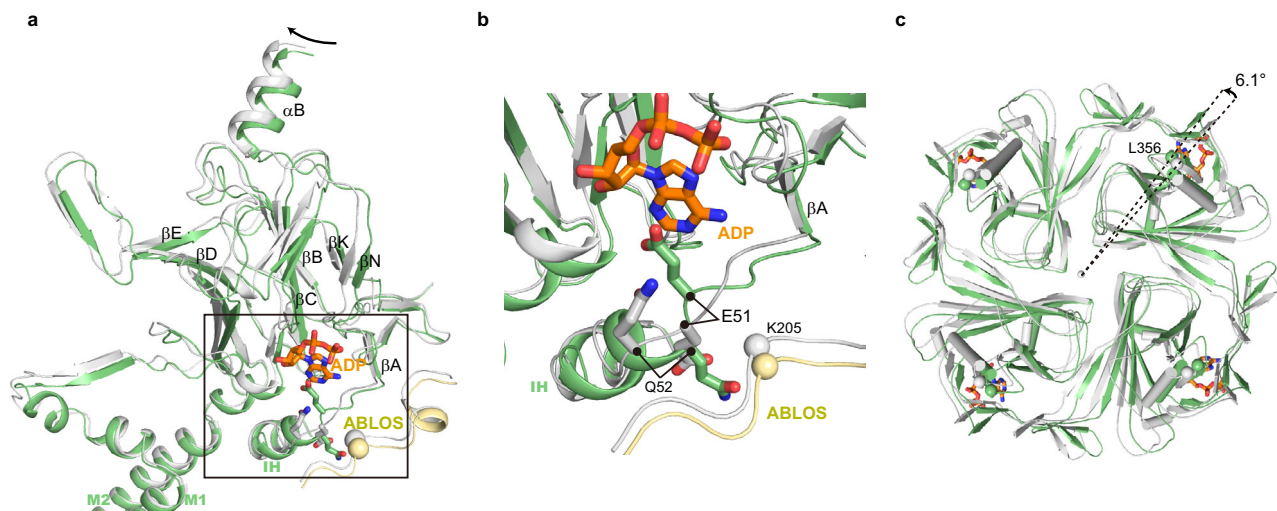

Fig. 3 Conformational changes of Kir6.2 CTD during K$_{ATP}$ channel opening. a Conformational changes of the nucleotide-binding site between the closed (gray) and the pre-open (green) states of H175K$_{cryo-EM}$. The ADP bound in the closed state is shown as sticks in orange. **b** Close-up view of the nucleotide-binding site boxed in (**a**). **c** Bottom view of the Kir6.2 CTD. The rotation angle between CTDs was measured using Cα positions of L356 of Kir6.2 as marker atoms (shown as spheres).
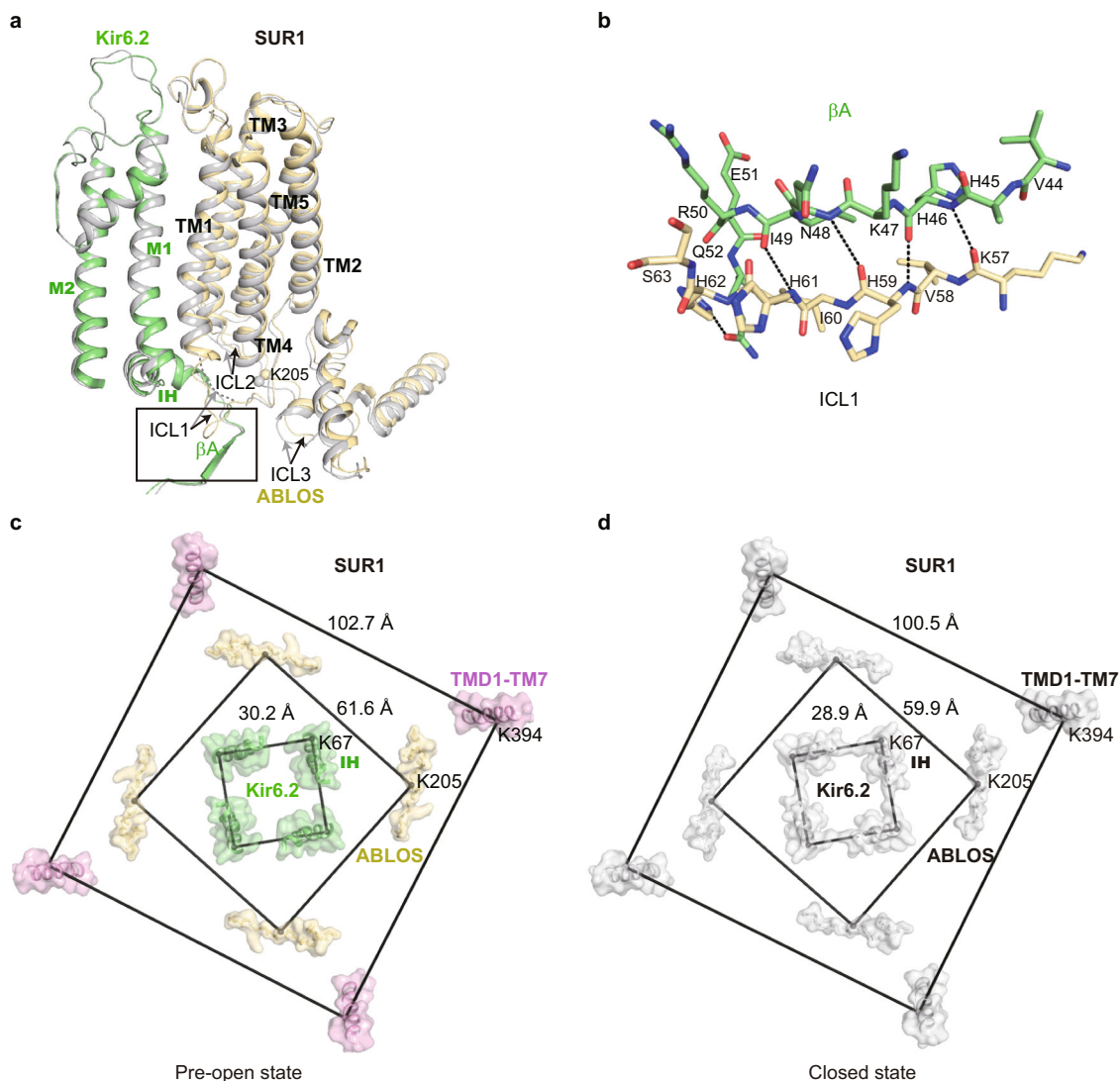
Fig. 4 Conformational changes of SUR1 during K_{ATP} channel opening. a Structural comparison of SUR1 TMD0 between the closed state (gray) and the pre-open state (colored) of H175K$_{cryo-EM}$. **b** Close-up view of the interaction between βA of Kir6.2 and SUR1-ICL1 boxed in (**a**). Putative hydrogen bondings are shown as dashes. **c**, **d** Bottom view of the structural arrangement of the K_{ATP} complex during channel opening. Cα positions of K67 on IH of Kir6.2, K205 on ABLOS of SUR1, and K397 on M7 of SUR1 are shown as spheres. Distances of marker atoms in the pre-open state (colored) and the closed state (gray) are shown in (**c**, **d**), respectively.

H175K$_{cryo-EM}$, we found K205 is away from ADP and does not form interactions with β phosphate of ADP (Fig. 4a, c, d and Supplementary Fig. 4 and Supplementary Movie 1). Moreover, the side-chain densities of residues on the ABLOS motif are not well resolved, indicating their high mobility. By measuring the distances between marker atoms of adjacent subunits, we found coordinated outward movements of Kir6.2 M1 helices (using Cα of Kir6.2 K67 as marker atoms), the ABLOS motif (using Cα of SUR1 K205 as marker atoms), and SUR1 ABC transporter module (using Cα of SUR1 K394 as marker atoms) (Fig. 4c, d).

KCO binds inside the SUR1 subunit in the NBD-dimerized conformation. The ABC transporter module of SUR1 shows an asymmetric NBD-dimerized structure as observed previously[22,26] (Fig. 5a). We observed that Mg-ADP is bound in the partially closed consensus site, while Mg-ATP is bound in the fully closed degenerate site (Fig. 5b, c). Since we did not supplement additional ATP into the cryo-EM sample, the ATP molecules might be carried through purification. The excellent local map quality

allowed us to unambiguously identify the NN414 molecule and to determine its binding pose (Fig. 5d).

NN414 binds inside the transmembrane domain of the SUR1 subunit. The dioxide group and its adjacent nitrogen atom of NN414 form polar interactions with H584 on TM11 (Fig. 5e–g). One NH group on the benzothiadiazine ring and the other NH group between benzothiadiazine ring and methylcyclopropyl group of NN414 form hydrogen bonds with D1031 on TM12 (Fig. 5e–g). Several hydrophobic interactions further stabilize the binding of NN414. The methylcyclopropyl group of NN414 forms hydrophobic interactions with M1290, Y1287, and T1286 on TM17 (Fig. 5e–g). The central benzothiadiazine ring of NN414 is sandwiched by C1072 of TM13, L1030 of TM12, and I552 of TM10 on one side and V555 of TM10 and L580 of TM11 on the other side (Fig. 5e–g). Rb$^+$ efflux assay showed that H584A or D1031A mutation does not impair K_{ATP} channel activation induced by metabolic inhibitors, indicating the correct folding and trafficking of these mutants to the plasma membrane, but these two mutations abolished the activation by NN414 in Rb$^+$ efflux assay (Fig. 5h, i). We further found the
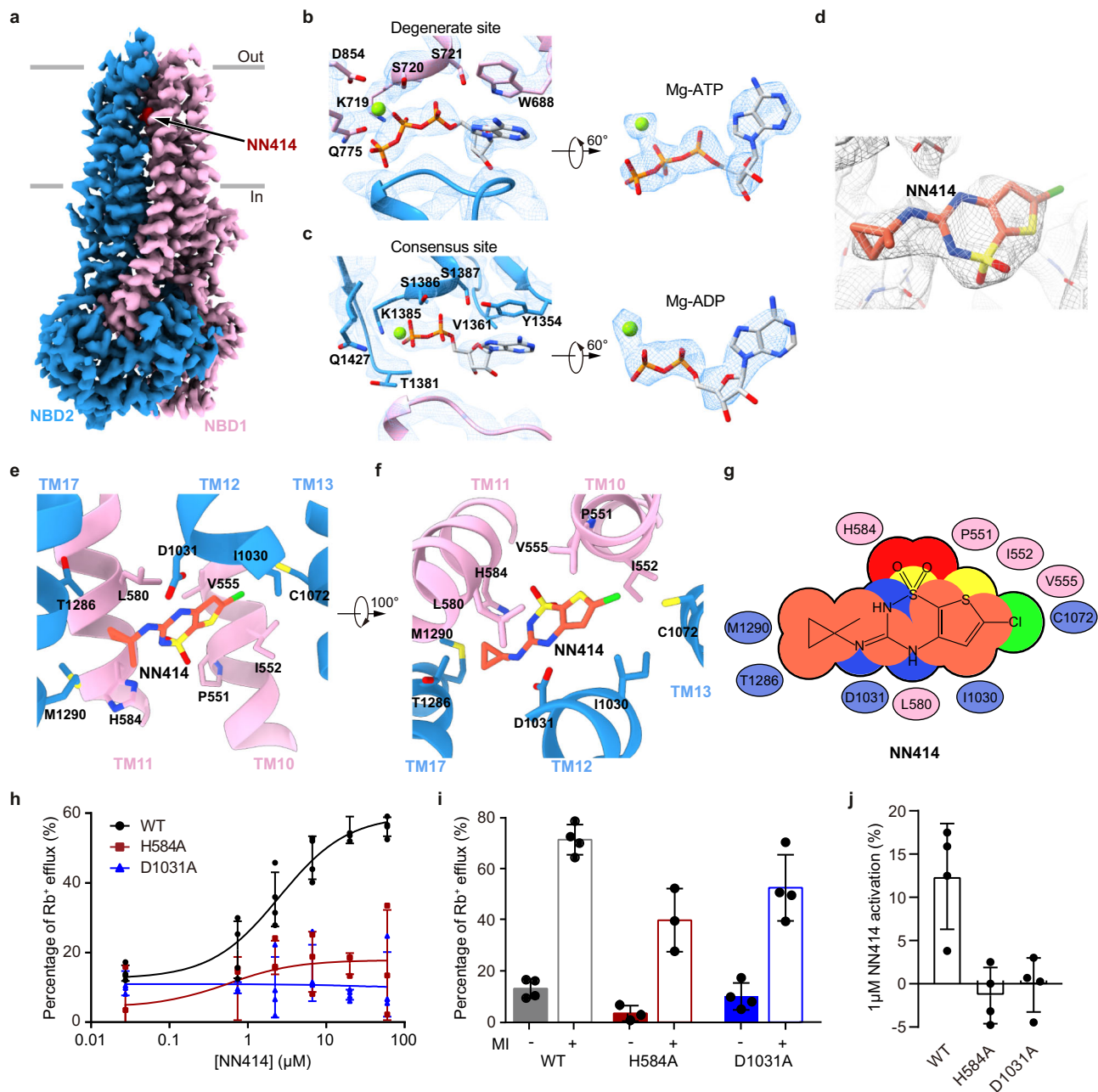
Fig. 5 Structure of the SUR1 subunit in complex with NN414 and Mg-nucleotides. a Cryo-EM density map of SUR1 in complex with Mg-nucleotides and NN414, viewed from the side. The approximate position of the lipid bilayer is indicated by gray bars. TMD1-NBD1, TMD2-NBD2, and NN414 are colored in pink, blue and red, respectively. For better visualization of the position of NN414, a fragment of TMD2 in front of NN414 was omitted. **b** Close-up views of electron densities at the degenerate site. NBD1, NBD2, nucleotides, and Mg^{2+} are colored in pink, blue, gray, and green, respectively. **c** Electron densities at the consensus sites. **d** NN414 density (orange) in the SUR1 subunit (gray). The map is shown as mesh and the protein is shown as sticks. **e**, **f** Close-up views of the NN414-binding site. TMD1 and TMD2 are colored in pink and blue, respectively. NN414 (orange) and residues that interact with NN414 are shown as sticks. **g** Cartoon representation of the interaction between NN414 and SUR1. The key residues on TMD1 and TMD2 are shown as pink and blue ovals, respectively. **h** The dose-response activation curves of SUR1- Kir6.2 K_{ATP} channel by NN414 measured by Rb^+ efflux assay. Curves were fitted to the Hill equation. Data are shown as mean ± SD and WT and D1031A $n = 4$, H584A $n = 3$ independent Rb^+ efflux assays, respectively. **i** Effects of metabolism inhibitors (MI) on K_{ATP} channel containing various SUR1 mutants. Data are shown as mean ± SD and WT and D1031A $n = 4$, H584A $n = 3$ independent Rb^+ efflux assays corresponding to (**h**). **j** K_{ATP} channel activation by 1 μM NN414 in the presence of 0.1 mM Mg-ATP. Data are shown as mean ± SD and $n = 3$ independent patches. Source data are provided as a Source Data file.

activation of K_{ATP} channel by NN414 in the presence of Mg-ATP is also abolished by H584A or D1031A as measured in the inside-out patch clamp mode, suggesting their essential role in the activation process of NN414 (Fig. 5j and Supplementary Fig. 6a–c).

Discussion

During the preparation of this manuscript, another group reported the K_{ATP} structure composed of SUR1-Kir6.2 double mutant (C166S, G334D)[29], abbreviate as C166S + G334D$_{cryo-EM}$. The C166S + G334D$_{cryo-EM}$ resembles the pre-open state

structure presented here, with RMSD of 0.34 Å in the Kir6.2 channel (Supplementary Fig. 7a, b). Moreover, both the $C166S + G334D_{cryo-EM}$ and $H175K_{cryo-EM}$ structures show a "propeller" architecture, which is similar to our previous structures of pancreatic K_{ATP} in the presence of ATP + RPG[27], ATP + GBM, or Mg-ADP + NN414[26]. The "propeller" architecture is dramatically different from the "quatrefoil" structure of pancreatic K_{ATP} observed in amphipol[22] or the vascular K_{ATP} observed in detergent[36]. The "propeller" architecture allows the communications between the ABC transporter module of SUR and Kir6 through the ICL3 (L0), which might be crucial for the nucleotide regulation of the K_{ATP} channel. In great contrast, the ICL3 is completely disordered in the "quatrefoil" structures. The physiological relevance of the "quatrefoil" structure awaits further investigation. In many K_{ATP} structures[26,27], we observed two conformations of Kir6.2 CTD, designated as "R" state and "T" state. There is a 12–13° anti-clockwise rotation from the "R" state to the "T" state viewed from the cytosolic side. These structures are similar to the Kir3.2 structure which shows "undocked state" (similar to "R" state) in the absence of $PI(4,5)P_2$ or docked state (similar to "T" state) in the presence of $PI(4,5)P_2$[31]. In the current work, we present the structures of $H175K_{cryo-EM}$ at both closed state and pre-open state. The CTD of $H175K_{cryo-EM}$ in the closed state is in a similar position to the "T" state of ATP + RPG structure (PDB ID: 6JB1) (Supplementary Fig. 4c). While the CTD of the pre-open structure has an additional 6° anti-clockwise rotation compared to the "T" state (Fig. 3c). These structural observations support the idea that K_{ATP} opening is associated with the rotation of Kir6.2 CTD, similar to that proposed for Kir2.2[30] or Kir3.2 channel[31], indicating a conserved "rotate to open" mechanism for Kir channel gating.

The cryo-EM density maps showed that in the same sample, inhibitory nucleotides exclusively bind Kir6.2 in the closed state but not in the open state. Further structural analysis revealed that the conformational changes of Kir6.2 during channel opening, including rotation of CTD and structural rearrangement of the βA-IH loop, disrupt the inhibitory nucleotide-binding pocket of Kir6.2 (Fig. 3a, b). Conversely, the wedging of nucleotide inside the nucleotide-binding pocket of the Kir6.2 channel would block conformational changes that are required for channel opening, providing a plausible mechanism for Kir6.2 channel inhibition by nucleotides. The signals of nucleotide-binding in Kir6.2 CTD are further transmitted to the central ion channel pore via several structural elements, including CTD, βA-IH loop, IH, and M2 gating helix (Fig. 3a). Corroborating with our observations, these structural elements are hotspots for genetic mutation of neonatal diabetes outside the ATP-binding pocket, such as E51, Q52, and G53 on βA-IH linker; V59, F60, and V64 on IH helix; A161, L164, C166, I167 and K170 on M2 (Supplementary Fig. 5)[5], suggesting that mutations in these structural elements might allosterically affect ATP inhibition and channel gating.

The binding of Mg-ADP to SUR1 induces the asymmetric dimerization of NBD1 and NBD2, which further drives the closure between TMD1 and TMD2 of the SUR1 ABC transporter module. Our structure shows that diazoxide-type K_{ATP} openers, exemplified by NN414, interact with both TMD1 and TMD2 (Fig. 5) to promote the closure of TMD (Fig. 6). The converged structural changes induced by Mg-ADP and K_{ATP} openers suggest their synergistic effect on K_{ATP} activation. Moreover, by aligning the structures of SUR1 in the presence and absence of NN414[29], we found NN414 binding induced the enlargement of its binding site surrounded by TM10, TM11, TM12, TM14, and TM17 (Supplementary Fig. 7c), suggesting an induced-fit mechanism for NN414 binding on SUR1.

Comparing the structure of K_{ATP} in the presence of ATP + RPG (PDB ID: 6JB1)[27] with the structure of $H175K_{cryo-EM}$ in the closed state (Supplementary Fig. 4a, b and Supplementary Movie 2), we found that their Kir6.2 channels are all in the same nucleotide-bound inhibited conformation (Supplementary Fig. 4c and Supplementary Movie 2). In contrast, there is a large structural rearrangement of SUR1 due to Mg-ADP and NN414 binding (Supplementary Fig. 4d–f and Supplementary Movie 2). The conformational changes of the ABC transporter module are transmitted to the lasso motif and finally arrive at TMD0, resulting in outward tilting of the inner half of TMD0 (Supplementary Fig. 4d–f, Supplementary Movie 1, and Supplementary Movie 2). Notably, the important ATP-coordinating residue K205 on the ABLOS motif of SUR1[27] moves outward and is away from the inhibitory nucleotide bound on the Kir6.2 (Supplementary Fig. 4d–f, and Supplementary Movie 1). This would certainly weaken the binding of inhibitory nucleotides and in turn, promote channel activation (Fig. 6a, b and Supplementary Movie 1). During the opening of Kir6.2, there is a further outward tilting of TMD0 and its associated intracellular loops, leaving more space for the expansion of Kir6.2 TMD (Figs. 4 and 6b, c and Supplementary Movie 1). Together with the outward movement of the ABLOS motif on SUR1 ICL3 where E203 locates (Fig. 4), there is a dramatic flipping movement of Q52 on βA-IH of Kir6.2 (Fig. 3). It is reported that Q52E mutation of Kir6.2 paired with E203K of SUR1 mutation greatly enhances the ATP sensitivity of K_{ATP}, and oxidative crosslinking of Q52C (Kir6.2) and E203C (SUR1) mutant could lock the channel in a closed state[37]. Our structural observation suggests that double mutations of Q52C and E203C, on one hand, block the opening conformational change of Kir6.2 directly and, on the other hand, fix the relative distance between the SUR1 ABLOS motif and Kir6.2 to inhibit channel opening.

Kir6 N-terminal peptide (KNtp) plays important role in regulating K_{ATP} function[38]. KNtp not only enhances the ATP sensitivity of Kir6.2 but also mediates the inhibition of insulin secretagogue in the absence of nucleotides, possibly by binding to the central vestibule of SUR and restraining the mobility of Kir6 CTD (Fig. 6a)[36,38]. In the $H175K_{cryo-EM}$ construct, the KNtp is covalently fused to the C-terminus of SUR1 and therefore could not bind inside the SUR1 central vestibule anymore[26,27]. However, the $H175K_{cryo-EM}$ construct could be inhibited by ATP and activated by Mg-ADP, as wild-type K_{ATP} channel (Supplementary Fig. 1d). Therefore, our current work uncovers the KNtp-independent nucleotide regulation mechanism of K_{ATP} channels (Fig. 6). Notably, the protein of $C166S + G334D_{cryo-EM}$ has free KNtp, but no density of KNtp is observed in the cryo-EM maps[29], supporting the hypothesis that KNtp is released from its binding site inside the central cavity of SUR1 and is flexible when the NBDs of SUR1 are dimerized (Fig. 6). Although the ion permeation pathway of the pre-open state does not allow the permeation of fully hydrated potassium ions (Fig. 2e), the hallmarks of K_{ATP} channel activation, such as the enlargement of inner helix gate of Kir6.2, the dissociation of inhibitory nucleotide from Kir6.2, the rotation of Kir6.2 CTD, and the binding of activator NN414 and activatory Mg-nucleotides on NBD-dimerized SUR1, all suggest the current pre-open structure represents the "activated" state of K_{ATP}. It is reported that the open probability of K_{ATP} is less than 100% in the activated condition[39], suggesting that K_{ATP} can sample the non-conductive activated state, which might be represented by the current pre-open structure.

Methods

Cell lines. FreeStyle 293 F (Thermo Fisher Scientific) suspension cells were cultured in SMM 293-TI (Sino Biological Inc.) supplemented with 1% FBS at 37 °C, with 6% CO_2 and 70% humidity. Sf9 insect (Thermo Fisher Scientific) cells were cultured in Sf-900 III SFM medium (Thermo Fisher Scientific) at 27 °C. AD293 cells (Agilent) were cultured in DMEM basic (Thermo Fisher Scientific)
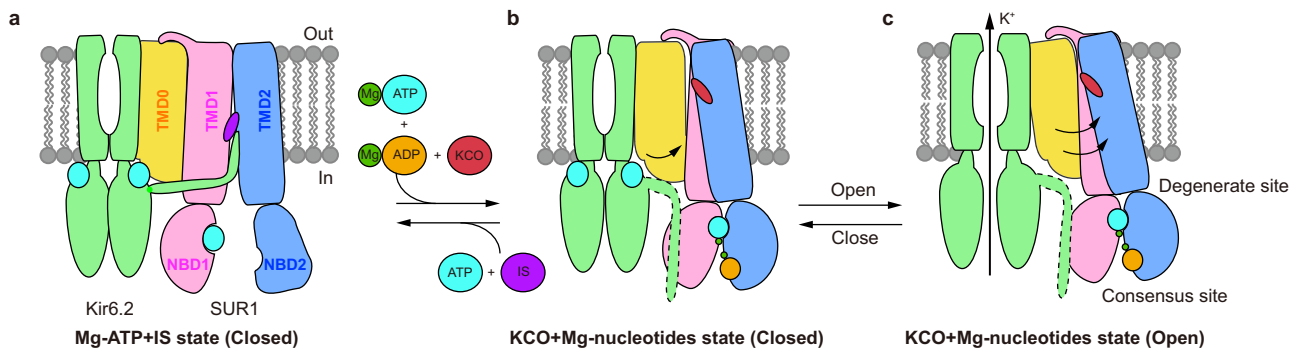
Fig. 6 Model for the K_ATP channel activation by Mg-nucleotides and K_ATP opener. a–c Side view of the cartoon model of the K_ATP channel. For simplicity, a pair of Kir6 subunits and one SUR2 subunit are shown. Kir6, TMD0, TMD1-NBD1, TMD2-NBD2, Mg^{2+}, ATP, ADP, insulin secretagogue (IS), and K_ATP opener (KCO) are colored in green, yellow, pink, blue, dark green, cyan, orange, purple, and red, respectively. The flexible KNtp in the Mg-nucleotide and K_ATP opener-bound state is outlined by dashed lines.

supplemented with 10% fetal bovine serum (FBS) at 37 °C, with 6% CO_2 and 70% humidity.

Construct of H175K_cyro-EM. We used cDNA of SUR1 from *Mesocricetus auratus* (maSUR1) and cDNA of Kir6.2 from *Mus musculus* (mmKir6.2) for our studies. We made a maSUR1-mmKir6.2 H175K fusion construct (H175K_cryo-EM) which is similar to our previous K_ATP fusion construct[26]. There were a 41-residue linker (VDGSGSGSGSGSAAGSGSGSGSGSGSGAAGSGSGSGSGSGSGSGAAALE) and an 8-residue Prescission Protease cleavage site (LEVLFQGP) between SUR1 and Kir6.2 H175K mutant. The first Met of Kir6.2 was removed to minimize internal translation initiation. This construct contains C-terminal GFP tag and strep tag which were used for protein purification. For electrophysiological experiments, Kir6.2 was cloned into a modified C-terminal GFP-tagged BacMam expression vector and SUR1 into non-tag BacMam expression vector as described previously[26].

Electrophysiology. K_ATP constructs were transfected into FreeStyle 293 F cells using polyethylenimine at the cell density of $0.8–1.1 \times 10^6$ cells/ml. Cells were cultured in 293TI medium supplemented with FBS for 24–36 h before recording. Macroscopic currents were recorded in inside-out mode at +60 mV via Axon-patch 200B amplifier (Axon Instruments, USA). Patch electrodes were pulled by a horizontal microelectrode puller (P-1000, Sutter Instrument Co, USA) to 2.0–5.0 MΩ resistance. In inside-out mode, both pipette and bath solution were KINT buffer, containing (mM): 140 KCl, 1 EGTA and 10 HEPES (pH 7.4, KOH). For neomycin activation, the 50 mM stock neomycin (Sigma) was made in DMSO, stored at −20 °C and diluted into KINT buffer to the desired concentration. For NN414 activation, the 50 mM NN414 stock (Sigma) was dissolved in DMSO, stored at −20 °C and diluted into KINT buffer to final working concentration. ATP and ADP stocks were prepared on ice, aliquoted and stored at −20 °C. ATP and ADP were dissolved in water and adjusted to pH 7 by KOH. The nucleotide concentration was determined by its extinction coefficient and the UV absorption at 259 nm. Recordings were acquired at 5 kHz and low-pass filtered at 1 kHz. Data were further analyzed by pClampfit 10.0 software. The fraction of NN414 activation was calculated as the ratio of the NN414-activated currents over the total currents of K_ATP channel.

Rb⁺ efflux assay. AD293 cells were cultured in six-well plate till 90–95% confluence. Wild type mmKir6.2 with C terminal GFP tag was co-transfected with wild type maSUR1 or maSUR1 with H584A mutation into AD293 cells. Cells were continually cultured for 24 h for protein expression and assembly, and GFP signal was detected by microscope in vivo. Then cells were digested by 0.25% trypsin supplemented with EDTA and were equally separated into 96-well plate, finally incubated with 100 μl medium per well. For Rb⁺ efflux determination, 6 mM Rb⁺ was supplemented into the medium for Rb⁺ pre-incubation in the cells. The 96-well plate was pre-treated by polylysine for about 24 h in 37 °C, and washed out by DMEM medium without FBS before incubation cells. After incubation in 96-well plate for 12–14 h, cells were washed by Ringer's solution (mM): 118 NaCl, 10 HEPES (pH 7.4), 25 NaHCO₃, 4.7 KCl, 1.2 KH₂PO₄, 2.5 CaCl₂, and 1.2 MgSO₄ and incubated with Ringer's solution supplemented with NN414 in different concentration for 10 min. As a baseline control, plasmids expressing GFP were transfected into cells at the same time. To detect whether K_ATP channels were functionally expressed, metabolic inhibitors including 3 mM de-O-glucose and 1 μM oligomycin were used to activate K_ATP channels. After drug treatment, the supernatants were transferred for Rb⁺ efflux determination. The cells plated in the well were dissolved by 1% Triton X-100 for 30 min and also transferred for total Rb⁺ quantification. The quantification of Rb⁺ was carried out on Ion Channel Reader 8000 (Aurora Group Company).

Protein expression and purification. K_ATP channels were expressed as described previously and the purification process was carried out with minor modification[26]. For protein purification, membrane pellets were homogenized in TBS (20 mM Tris-HCl pH 7.5, 150 mM NaCl) and solubilized in TBS with 1% digitonin (bio-synth), supplemented with protease inhibitors (1 mg/ml Leupeptin, 1 mg/ml Pep-statin, 1 mg/ml Aprotinin, and 1 mM PMSF), 1 mM EDTA and 1 mM EGTA for 30 min at 4 °C. Unsolubilized materials were removed after centrifugation at 100,000 g for 30 min and the supernatant was loaded onto two 5 mL columns packed with Streptactin 4FF resin (Smart Lifesciences). Strep column was first washed by TBS buffer supplemented with 0.1% digitonin, protease inhibitors (1 mg/ml Leupeptin, 1 mg/ml Pepstatin, 1 mg/ml Aprotinin), 1 mM EDTA and 1 mM EGTA. Then the columns were washed with TBS supplemented with 0.1% digitonin, 3 mM MgCl₂ and 1 mM ATP. The last washing step buffer was TBS supplemented with 0.1% digitonin. The K_ATP octamers were eluted by TBS supplemented with 0.1% digitonin and 8 mM desthiobiotin. The eluate was concentrated and loaded onto Superose 6 increase column (GE Healthcare) running with TBS supplemented with 0.1% digitonin. Peak fractions were collected and concentrated to $A_{280} = 15$ (estimated as 15 μM K_ATP octamers). The protein purification was completed within 15 h and the purified protein was instantly used for cryo-EM sample preparation.

Cryo-EM sample preparation. K_ATP octamers were supplemented with 5 mM MgCl₂, 0.5 mM ADP, 0.5 mM NN414 and 10 μM PI(4,5)P₂diC₈. Acidic PI(4,5) P₂diC₈ (Echelon Biosciences) was dissolved in water and buffered by Tris-HCl (pH 7.5) before usage. The final protein concentration was estimated to be 13.5 μM octamer. Cryo-EM grids were prepared with Vitrobot Mark IV (FEI) and GIG R1/1 holey carbon grids, which were glow-discharged for 120 s using air before making Cryo-EM sample grids. 2.5 μl K_ATP octamers sample was applied to the glow-discharged grid and then the grid was blotted at blotting force in level 2 for 2 s at 100% humidity and 20 °C, before plunge-frozen into the liquid ethane.

Cryo-EM data acquisition. Cryo-grids were screened on a Talos Arctica microscope (Thermo Fisher Scientific) operated at 200 kV for small-scale data collection. For grids of high quality, a large data set for K_ATP channel structure determination was collected in Titan Krios microscope (Thermo Fisher Scientific) operated at 300 kV.

Images were collected using K2 camera (Gatan) which was mounted post a Quantum energy filter with 20 eV slit, operated under super-resolution mode with a pixel size of 1.324 Å at the object plane, and controlled by Serial EM. Defocus values were set to range from −1.3 μm to −1.8 μm for data collection. The dose rate on detector was 8 e⁻s⁻¹A⁻². And the total exposure was 50 e⁻/A². Each 12 s movie was dose-fractioned into 50 frames.

Image processing. Movies collected were exposure-filtered, gain-corrected, motion-corrected, mag-distortion-corrected and binned with MotionCor2-1.3.2[40], producing dose-weighted and summed micrographs with pixel size 1.324 Å. CTF models of dose-weighted micrographs were determined using Gctf-1.18[41]. Gautomatch-0.56 (developed by Kai Zhang, MRC-LMB) was used for particles auto-picking and Gautomatch-0.56 templates were produced by projecting K_ATP density map generated from small-scale data collected from 200 kV microscope. Data processing was initially executed in Relion_3.1[42]. Particles were extracted from dose-weighted micrographs. After 2 rounds of 2D classification and 3D classification with C4 symmetry, particles of good quality were re-extracted and re-centered. The remaining particles were used for 3D refinement and CTF refinement. Upon convergence, the particles were expanded using C4 symmetry and signals for the SUR1 ABC transporter module were subtracted. The subtracted particles were refined using local search within 5° range. The refined SUR1 ABC

transporter particles were subjected to no alignment 3D classification, with K = 4 and T = 20. The 3D classes with good map quality were selected and refined in cryoSPARC-3.1.0 by non-uniform refinement[43], CTF refinement and local non-uniform refinement to reach a resolution of 3.11 Å (map-A). Focused 3D classification on Kir6.2 CTD was carried out with K = 4 and T = 20 without alignment. Two 3D classes with good features but with relative rotations were selected and refined using non-uniform refinement, CTF refinement and local non-uniform refinement in cryoSPARC-3.1.0 to generate consensus maps. Examination of their pore domain revealed they represent the pre-open state and the closed state respectively. With the mask of Kir6.2 for local refinement, the resolution of the pre-open state reached 2.87 Å (map-B) and the closed state reached 3.16 Å (map-C). With the mask for Kir6.2 TMD and SUR1 TMD0, the resolution of the pre-open state reached 2.94 Å (map-D) and the resolution of the closed state reached 3.19 Å (map-E). The sharpened local refined maps were aligned to the consensus map and summed by vop maximum command in UCSF chimera-1.14 to generate composite maps. Specifically, we summed map-A, map-B and map-D to generate pre-open state map and map-A, map-C and map-E to generate closed state map. The composite cryo-EM maps were reboxed to 180 × 180 × 180 and used for interpretation, model building, refinement and illustration.

Model building. The structure of K_{ATP} in complex with ATP and RPG (PDB ID: 6JB1)[27] or Mg-ADP and NN414 (PDB ID: 5YWC)[26] was divided into individual domains and fitted into the cryo-EM maps using UCSF chimera-1.14[44]. The model was further manually rebuilt in Coot-0.8.6 and refined against the maps using Phenix version 1.18-3777[45]. Permeation pathways were calculated using HOLE2[46].

Quantification and statistical analysis. Global resolution estimations of cryo-EM density maps are based on the 0.143 Fourier Shell Correlation criterion[47]. The local resolution map was calculated using cryoSPARC[48]. Rb^+ efflux assay curves were fitted to the Hill equation using GraphPad Prism 5. Electrophysiological data reported were analyzed with pclampfit 10.0 software. The number of biological replicates (N) and the relevant statistical parameters for each experiment (such as mean or standard error) are described in figure legends. No statistical methods were used to pre-determine sample sizes.

Figure preparation. Figures were prepared using the programs UCSF Chimera X-0.91 (http://www.rbvi.ucsf.edu/chimerax/54)[49], UCSF Chimera-1.14 (http://www.cgl.ucsf.edu/chimera/48), and PyMOL-1.7.0.5 (http://www.pymol.org/).

Reporting summary. Further information on research design is available in the Nature Research Reporting Summary linked to this article.

Data availability

References

1. Nichols, C. G. KATP channels as molecular sensors of cellular metabolism. *Nature* **440**, 470–476 (2006).
2. Ashcroft, F. M. K(ATP) channels and insulin secretion: a key role in health and disease. *Biochem. Soc. Trans.* **34**, 243–246 (2006).
3. Vishwakarma, V. K. et al. Mechanistic Pathways of ATP Sensitive Potassium Channels Referring to Cardio-Protective Effects and Cellular Functions. *Drug Res. (Stuttg.)* **69**, 365–373 (2019).
4. Brayden, J. E. Functional roles of KATP channels in vascular smooth muscle. *Clin. Exp. Pharmacol. Physiol.* **29**, 312–316 (2002).
5. Pipatpolkai, T., Usher, S., Stansfeld, P. J. & Ashcroft, F. M. New insights into KATP channel gene mutations and neonatal diabetes mellitus. *Nat. Rev. Endocrinol.* **16**, 378–393 (2020).
6. Bienengraeber, M. et al. ABCC9 mutations identified in human dilated cardiomyopathy disrupt catalytic KATP channel gating. *Nat. Genet.* **36**, 382–387 (2004).
7. Olson, T. M. et al. KATP channel mutation confers risk for vein of Marshall adrenergic atrial fibrillation. *Nat. Clin. Pract. Cardiovasc. Med.* **4**, 110–116 (2007).
8. Harakalova, M. et al. Dominant missense mutations in ABCC9 cause Cantu syndrome. *Nat. Genet.* **44**, 793–796 (2012).
9. van Bon, B. W. et al. Cantu syndrome is caused by mutations in ABCC9. *Am. J. Hum. Genet.* **90**, 1094–1101 (2012).
10. Smeland, M. F. et al. ABCC9-related Intellectual disability Myopathy Syndrome is a KATP channelopathy with loss-of-function mutations in ABCC9. *Nat. Commun.* **10**, 4457 (2019).
11. Bryan, J., Crane, A., Vila-Carriles, W. H., Babenko, A. P. & Aguilar-Bryan, L. Insulin secretagogues, sulfonylurea receptors and K(ATP) channels. *Curr. Pharm. Des.* **11**, 2699–2716 (2005).
12. Jahangir, A. & Terzic, A. K(ATP) channel therapeutics at the bedside. *J. Mol. Cell. Cardiol.* **39**, 99–112 (2005).
13. Miki, T., Nagashima, K. & Seino, S. The structure and function of the ATP-sensitive K+ channel in insulin-secreting pancreatic beta-cells. *J. Mol. Endocrinol.* **22**, 113–123 (1999).
14. Tucker, S. J., Gribble, F. M., Zhao, C., Trapp, S. & Ashcroft, F. M. Truncation of Kir6.2 produces ATP-sensitive K+ channels in the absence of the sulphonylurea receptor. *Nature* **387**, 179–183 (1997).
15. Baukrowitz, T. et al. PIP2 and PIP as determinants for ATP inhibition of KATP channels. *Science* **282**, 1141–1144 (1998).
16. Shyng, S. L. & Nichols, C. G. Membrane phospholipid control of nucleotide sensitivity of KATP channels. *Science* **282**, 1138–1141 (1998).
17. Hilgemann, D. W. & Ball, R. Regulation of cardiac Na+,Ca2+ exchange and KATP potassium channels by PIP2. *Science* **273**, 956–959 (1996).
18. Fan, Z. & Makielski, J. C. Anionic phospholipids activate ATP-sensitive potassium channels. *J. Biol. Chem.* **272**, 5388–5395 (1997).
19. Schwanstecher, C., Dickel, C. & Panten, U. Interaction of tolbutamide and cytosolic nucleotides in controlling the ATP-sensitive K+ channel in mouse beta-cells. *Br. J. Pharmacol.* **111**, 302–310 (1994).
20. Aittoniemi, J. et al. Review. SUR1: a unique ATP-binding cassette protein that functions as an ion channel regulator. *Philos. Trans. R. Soc. Lond. B. Biol. Sci.* **364**, 257–267 (2009).
21. Moreau, C., Prost, A. L., Derand, R. & Vivaudou, M. SUR, ABC proteins targeted by KATP channel openers. *J. Mol. Cell. Cardiol.* **38**, 951–963 (2005).
22. Lee, K. P. K., Chen, J. & MacKinnon, R. Molecular structure of human KATP in complex with ATP and ADP. *Elife* **6**, https://doi.org/10.7554/eLife.32481 (2017).
23. Li, N. et al. Structure of a Pancreatic ATP-Sensitive Potassium Channel. *Cell* **168**, 101–110 (2017).
24. Martin, G. M., Kandasamy, B., DiMaio, F., Yoshioka, C. & Shyng, S. L. Anti-diabetic drug binding site in a mammalian KATP channel revealed by Cryo-EM. *Elife* **6**, https://doi.org/10.7554/eLife.31054 (2017).
25. Martin, G. M. et al. Cryo-EM structure of the ATP-sensitive potassium channel illuminates mechanisms of assembly and gating. *Elife* **6**, https://doi.org/10.7554/eLife.24149 (2017).
26. Wu, J. X. et al. Ligand binding and conformational changes of SUR1 subunit in pancreatic ATP-sensitive potassium channels. *Protein Cell* **9**, 553–567 (2018).
27. Ding, D., Wang, M., Wu, J. X., Kang, Y. & Chen, L. The Structural Basis for the Binding of Repaglinide to the Pancreatic KATP Channel. *Cell Rep.* **27**, 1848–1857 e1844 (2019).
28. Martin, G. M. et al. Mechanism of pharmacochaperoning in a mammalian KATP channel revealed by cryo-EM. *Elife* **8**, https://doi.org/10.7554/eLife.46417 (2019).
29. Zhao, C. & MacKinnon, R. Molecular structure of an open human KATP channel. *Proc. Natl. Acad. Sci. U. S. A.* **118**, https://doi.org/10.1073/pnas.2112267118 (2021).
30. Hansen, S. B., Tao, X. & MacKinnon, R. Structural basis of PIP2 activation of the classical inward rectifier K+ channel Kir2.2. *Nature* **477**, 495–498 (2011).
31. Niu, Y., Tao, X., Touhara, K. K. & MacKinnon, R. Cryo-EM analysis of PIP2 regulation in mammalian GIRK channels. *Elife* **9**, https://doi.org/10.7554/eLife.60552 (2020).
32. Haider, S., Tarasov, A. I., Craig, T. J., Sansom, M. S. & Ashcroft, F. M. Identification of the PIP2-binding site on Kir6.2 by molecular modelling and functional analysis. *EMBO J.* **26**, 3749–3759 (2007).
33. Carr, R. D., Brand, C. L., Bodvarsdottir, T. B., Hansen, J. B. & Sturis, J. NN414, a SUR1/Kir6.2-selective potassium channel opener, reduces blood glucose and improves glucose tolerance in the VDF Zucker rat. *Diabetes* **52**, 2513–2518 (2003).
34. Zheng, X. et al. Mechanism of ligand activation of a eukaryotic cyclic nucleotide-gated channel. *Nat. Struct. Mol. Biol.* **27**, 625–634 (2020).
35. Israelachvili, J. N. in *Intermolecular and Surface Forces* (Third Edition) (ed J. N. Israelachvili) 71–90 (Academic Press, 2011).
36. Sung, M. W. et al. Vascular KATP channel structural dynamics reveal regulatory mechanism by Mg-nucleotides. *Proc. Natl. Acad. Sci. U. S. A.* **118**, https://doi.org/10.1073/pnas.2109441118 (2021).
37. Pratt, E. B., Zhou, Q., Gay, J. W. & Shyng, S. L. Engineered interaction between SUR1 and Kir6.2 that enhances ATP sensitivity in KATP channels. *J. Gen. Physiol.* **140**, 175–187 (2012).

38. Wu, J. X., Ding, D., Wang, M. & Chen, L. Structural Insights into the Inhibitory Mechanism of Insulin Secretagogues on the Pancreatic ATP-Sensitive Potassium Channel. *Biochem. (Mosc.)* **59**, 18–25 (2020).

39. Proks, P., de Wet, H. & Ashcroft, F. M. Activation of the K(ATP) channel by Mg-nucleotide interaction with SUR1. *J. Gen. Physiol.* **136**, 389–405 (2010).

40. Zheng, S. Q. et al. MotionCor2: anisotropic correction of beam-induced motion for improved cryo-electron microscopy. *Nat. Methods* **14**, 331–332 (2017).

41. Zhang, K. Gctf: Real-time CTF determination and correction. *J. Struct. Biol.* **193**, 1–12 (2016).

42. Zivanov, J. et al. New tools for automated high-resolution cryo-EM structure determination in RELION-3. *Elife* **7**, https://doi.org/10.7554/eLife.42166 (2018).

43. Punjani, A., Zhang, H. & Fleet, D. J. Non-uniform refinement: adaptive regularization improves single-particle cryo-EM reconstruction. *Nat. Methods* **17**, 1214–1221 (2020).

44. Pettersen, E. F. et al. UCSF Chimera–a visualization system for exploratory research and analysis. *J. Comput Chem.* **25**, 1605–1612 (2004).

45. Afonine, P. V. et al. Real-space refinement in PHENIX for cryo-EM and crystallography. *Acta Crystallogr D. Struct. Biol.* **74**, 531–544 (2018).

46. Smart, O. S., Neduvelil, J. G., Wang, X., Wallace, B. A. & Sansom, M. S. HOLE: a program for the analysis of the pore dimensions of ion channel structural models. *J. Mol. Graph.* **14**, 354–360 (1996). 376.

47. Rosenthal, P. B. & Henderson, R. Optimal determination of particle orientation, absolute hand, and contrast loss in single-particle electron cryomicroscopy. *J. Mol. Biol.* **333**, 721–745 (2003).

48. Punjani, A., Rubinstein, J. L., Fleet, D. J. & Brubaker, M. A. cryoSPARC: algorithms for rapid unsupervised cryo-EM structure determination. *Nat. Methods* **14**, 290–296 (2017).

49. Pettersen, E. F. et al. UCSF ChimeraX: Structure visualization for researchers, educators, and developers. *Protein Sci.* https://doi.org/10.1002/pro.3943 (2020).

Author contributions

L.C. initiated the project. M.W. purified protein, prepared the cryo-EM sample, and performed electrophysiology experiments. D.D. made mutants for SUR1. M.W. and J-X.W. collected the data. M.W. processed the data, built and refined the model with the help of L.C. All authors contributed to the paper preparation.

Competing interests

The authors declare no competing interests.

Additional information

Supplementary information The online version contains supplementary material available at https://doi.org/10.1038/s41467-022-30430-4.

Correspondence and requests for materials should be addressed to Lei Chen.

Peer review information *Nature Communications* thanks Konstantinos Beis, Michael Puljung and the other, anonymous, reviewer(s) for their contribution to the peer review of this work.

Reprints and permission information is available at http://www.nature.com/reprints

Publisher's note Springer Nature remains neutral with regard to jurisdictional claims in published maps and institutional affiliations.